Enhanced Gradient Crystal-Plasticity study of size effects in a β-titanium alloy

Murat Demiral[1], Kai Nowag[2], Anish Roy[3]*, Rudy Ghisleni[2], Johann Michler[2], Vadim V. Silberschmidt[3]

[1]Department of Mechanical Engineering, Çankaya University, 06810 Ankara, Turkey

[2]Laboratory for Mechanics of Materials and Nanostructures, EMPA - Swiss Federal Laboratories for Materials Science and Technology, Feuerwerkerstrasse 39, CH-3602 Thun, Switzerland

[3]Wolfson School of Mechanical, Electrical and Manufacturing Engineering, Loughborough University, LE11 3TU UK

* Corresponding author. Tel.: +44 1509 227 637; E-mail: A.Roy3@lboro.ac.uk

Abstract

A calibrated model of enhanced strain-gradient crystal plasticity is proposed, which is shown to characterize adequately deformation behaviour of b.c.c. single crystals of a β-Ti alloy (Ti-15-3-3-3). In this model, in addition to strain gradients evolving in the course of deformation, incipient strain gradients, related to a component's surface-to-volume ratio, is accounted for. Predictive capabilities of the model in characterizing a size effect in an initial yield and a work-hardening rate in small-scale components is demonstrated. The characteristic length-scale, i.e. the component's dimensions below which the size effect is observed, was found to depend on densities of polar and statistical dislocations and interaction between them.

Keywords: Strain gradient plasticity; Size effect; Single crystal; Titanium alloy; Micropillar compression

1. Introduction and motivation

There is a vast body of experimental evidence that demonstrate that the deformation mechanisms at the micron or sub-micron scales are dramatically different than that of macro-scale [1-5]. In several of these pioneering studies, the size-effect of the

mechanical properties has been attributed to non-uniform straining during the deformation process [1-6]. Thus, size effect was not expected under imposed homogeneous strain field, such as in micropillar compression tests. However, it has been reported consistently by several studies that a strong inverse relationship existed between yield stress and a diameter of the pillar [4,5,7,8].

To interpret the size effect in micron or sub-micron pillars, different mechanisms including dislocation starvation-dislocation nucleation [9], multiplication via a single-arm source operation [10,11], source truncation [10] and source exhaustion [12] as well as weakest-link theories [13] were proposed. The study of Norfleet et al. [12] demonstrated that the combination of other models such as lattice friction, source-truncation hardening and forest hardening was inadequate to explain large flow strengths in experiments, suggesting that other mechanisms might also affect the size effect. The presence of defects induced by focused ion beam (FIB) has led several researchers to infer that the fabrication process may play a significant role in the observed size effects [14,15]. However, the study of Jennings et al. [16] demonstrated that the observed size effects in small-size pillars were a function of microstructure rather than the fabrication technique.

The influence of microstructure on the size-effect was also studied. The experimental study of Maass and co-workers [17-19] demonstrated that a significant amount of geometrically necessary dislocations (GNDs) were generated in compression giving a rise to strain gradients. Numerical studies in [20-23] showed that macroscopically homogenous deformation was microscopically heterogeneous, i.e. the GND density vanished macroscopically but not locally. Maass et al. [24] studied the initial microstructure of undeformed Au, Ni, Cu and NiTi micropillars using white-beam Laue

micro-diffraction. The study revealed that strain gradients existed even in the initial microstructure of pillars, and the results suggested that a higher surface-to-volume ratio in small-size pillars raised the occurrence of pre-existing strain gradients. Recently, Fan et al. [25] and Hurtado and Ortiz [26] demonstrated the influence of free surfaces on the size effect using discrete-dislocation dynamics and a non-local continuum model, respectively. From a modelling standpoint, continuum modelling approaches based on the elastic theory of continuously distributed dislocations (ECDD) [27,28] has shown much promise in predicting several key mechanisms of small scale plasticity [29,30].

Here, an important note should be made with regard to terminology used in the text. A concept of *polar dislocations* (PDs) is introduced as a spatially averaged dislocation density that can be measured or characterised. This can be considered as a numerical dislocation density homogenised over a spatially finite (and small) volume along the lines of a volume-averaged Nye's tensor [31]. Naturally, spatial averaging cancels an effect of dislocations of opposite signs within the chosen volume. Such dislocations of opposing signs are referred to as *statistically distributed dislocations* (SDs) with a respective density. Thus, the difference between a true microscopic dislocation density (in the local sense) and the spatially averaged density of PDs is equal to the density of SDs. Thus, in essence, if the spatial window is small enough to resolve individual dislocations (the scale of discrete-dislocation mechanics), then all dislocations are referred to as PDs. We note that PDs can include aspects of GNDs linked with lattice incompatibility, but not exclusively. In our study, PDs are associated with the generation of long-range internal stresses [32]. Consequently, SDs are assumed to be arranged so as to render a net zero macroscopic stress field but with inter-dislocation interactions resulting in hardening. In conventional plasticity theories, only SDs are

considered. In our study, both species (PDs and SDs) contribute to plastic flow. The evolution processes of PDs and SDs are coupled, since spatial gradients in the plastic distortion field may generate PDs [33,34].

An enhanced model of strain-gradient crystal-plasticity (EMSGCP) is proposed, in which the initial microstructure of micro-pillars determines the value of critical resolved shear stress (*CRSS*) of slip systems as described in terms of PDs and SDs. The incipient strain gradients are correlated with the sample's surface-to-volume (*S/V*) ratio. The model is calibrated to capture the deformation charecteristics of B.C.C. single crystals of a β-Ti alloy, namely, Ti-15-3-3-3.

This paper is organized as follows. In Section 2 details of micro-pillar-compression experiments are presented. Section 3 introduces the theory of the enhanced modelling of strain-gradient crystal plasticity and Section 4 describes the steps followed to develop the FE model of the micro-pillar-compression test. In Section 5 we demonstrate the calibration of EMSGCP parameters followed by the numerical predictions for the size effect in micro-pillar-compression experiments with their associated discussions in Section 6. A parametric study on the underlying length-scale of the proposed model is presented in Section 7. The paper ends with some concluding remarks in Section 8.

2. Micro-pillar-compression experiments

Micro-pillar compression experiments were performed at Swiss Federal Laboratories for Materials Science and Technology (EMPA). Cylindrical micro-pillars with a diameter of ~1 μm and ones with square cross sections with an edge length of 0.9 μm to 2 μm were fabricated in single grains of a polycrystalline sample by using a dual beam FIB / SEM Tescan FIB Lyra instrument. The exact orientation of the grains along the compression axis of the micro-pillars were (0.538 0.532 0.652) for the cylindrical pillar

and (0.489 0.443 0.751) for the others. To find a compromise between a fabrication time and accuracy of the process, pillars were produced using different energies in consecutive fabrication steps. First a current of ~ 4 nA was used, followed by 0.15 nA and 0.79 nA to obtain the final shape for micro-pillars with an edge length of 1 µm and 2 µm respectively. The voltage was kept constant at 30 kV throughout.

All the compression tests were carried out inside a Zeiss DSM 962 scanning electron microscope (SEM), using a micro-indenter designed at EMPA in cooperation with the Institute of Materials Science, Swiss Federal Institute of Technology Lausanne [35,36], which allows a precise pillar-punch positioning and *in situ* characterization of deformation events. A flat punch tip was used to compress the pillars to achieve a homogenous uniaxial state of stress (this assumption is violated due to a taper in the pillars and misalignment between the punch and pillar as described in Section 5). All the pillars were compressed in a displacement-control mode at a strain-rate of ~ 10^{-4} s^{-1}. A Hitachi S4800 high-resolution SEM system was used for imaging the pillars before and after compression.

Active slip system was identified by comparing SEM pictures of the compressed pillar and pole-figures of the EBSD scan (Fig. 1). The slip direction was assigned by the projected direction of the motion of the top part of the pillar as indicated by the red arrow in Fig. 1a, b. This direction was identified to correspond exactly to the projection of the {111} direction, represented by an intersection point in the pole figure. The direction [1 $\bar{1}$ 1] was therefore found to be the active slip direction. Orientation of the active slip plane was indentified by the position of the line of intersection between the slip plane and the pillar surface, highlighted in Fig. 1b (green line). The intersection line was found by analysing deformation lines created when the top part of the pillar was

deformed, resulting in a large slip step visible in Fig. 1b. While several deformation lines were observed to the right of the intersection line parallel to the slip direction, no such deformation marks were observed to the left of the green line, indicating that the original pillar surface was still present in this area. However, as pole figures depict only crystallographic directions and no planes, the active slip plane was determined using a direction of its corresponding normal, as shown in Fig. 1c. As before, exactly one matching plane was found, and no compliance was achieved for other possible families of slip planes, namely {011} and {123}. Hence, the slip-plane normal was identified to be (121). The measured angle between the top face and slipped surface (Fig. 1d) of 30° is in excellent agreement with the theoretically calculated value of 29.7° between the surface orientation of the compressed crystal (0.489 0.443 0.751) and the active slip plane (121). A careful analysis was conducted for all pillars, and it was observed that, irrespective of the pillar size, deformation took place by single slip on the slip system $(121)[1\bar{1}1]$. This particular system exhibits a Schmid factor of 0.4, the highest of all possible slip systems of the {112} <111> type.

Fig. 1

Size-effect studies were conducted on nominally square pillars with varying cross-sectional area (Table 1). The effect of the surface-to-volume (S/V) ratio on average yield strength for all samples tested is summarized in the logarithmic plot shown in Fig. 2. Here, average yield stress ($\bar{\sigma}$) and strain ($\bar{\varepsilon}$) are defined as $|\sum RF_2|/A_p$ and $-\ln(L_p/L_0)$, respectively, where $|\sum RF_2|$ represents the reaction force in the y-direction corresponding to the applied displacement, A_p is the mid-height instantenous cross-sectional area of the pillar, and L_p and L_0 are the current and initial heights of the pillar, respectively. Here, we note that the definitions of average stress and strain are somewhat different from

those of true stress and strain. This is due to underlying inhomogeneity of the imposed stress field emanating from misalignment between the indenter tip and the pillar surface, geometrical parameters of the pillar, i.e. the pillar's taper and boundary conditions imposed on the bottom surface of the pillar to account for the influence of the substrate. It should be emphasized that only the pillar upper and side surfaces were considered in calculating the overall surface area to determine the S/V ratio since the bottom surface was attached to a substrate, i.e. not a free surface. Yield stress was observed to increase with the increasing S/V ratio and with the decreasing edge length, with a best fit line of $\sigma_{Y} \propto (S/V)^{0.684}$ and $\sigma_{Y} \propto (d_{\mathrm{eff}})^{-0.705}$, respectively (Fig. 2). The effective diameter, d_{eff}, was calculated by matching the cross-sectional area of the square pillar to that of a circular one: $d_{\mathrm{eff}} = 2l/\sqrt{\pi}$ [37]. The observed dependence is consistent with the one for Ni pillars, where $\sigma_{Y} \propto (d_{\mathrm{eff}})^{-0.69)}$ [38], but it is stronger than that for gold micropillars, $\sigma_{Y} \propto (d_{\mathrm{eff}})^{-0.60}$ [39].

Fig. 2

3. Enhanced model of strain-gradient crystal-plasticity theory

The following notations are used: a gradient operator is indicated by ∇ and incremental changes in variables due to temporal evolution of these by a Δ symbol. A bold symbol denotes a vector or a tensor and a dot superposed on a symbol indicates a time derivative. The operation $\times$ is a vector product. The summation convention is implied throughout. Subscripts P and S indicate PDs and SDs, respectively.

The proposed theory is an enhanced version of a strain-gradient crystal-plasticity theory (SGCP), and we review some of the fundamentals which motivate our approach. It should be emphasized that the SGCP theory considered here is the lower-order

mechanism-based strain-gradient crystal-plasticity theory (MBSGCP), originally proposed by Han et al. [40].

For completeness, constitutive relations of the MBSGCP theory are summarized below. In this elasto-visco-plastic crystal plasticity-based constitutive law, the stress rate $\dot{\sigma}_{ij}$ is related to the elastic strain rate $\dot{\varepsilon}_{kl}^{e}$ as

$$\dot{\sigma}_{ij} = C_{ijkl}\dot{\varepsilon}_{kl}^{e} = C_{ijkl}(\dot{\varepsilon}_{kl} - \dot{\varepsilon}_{kl}^{p}), \tag{1}$$

where C is the fourth-order elasticity tensor, $\dot{\varepsilon}_{ij}$ is the total strain rate and $\dot{\varepsilon}_{kl}^{p}$ is the plastic strain rate, calculated by

$$\dot{\varepsilon}_{ij}^{p} = \sum_{\alpha=1}^{N}\mu_{ij}^{\alpha}\dot{\gamma}^{\alpha}. \tag{2}$$

In Eq. (2) N is the total number of slip sytems, μ_{ij}^{α} is the Schmid factor and $\dot{\gamma}^{\alpha}$ is the shear strain rate in a slip system α. The viscoplastic power-law expression proposed by Hutchinson [41] was used to describe $\dot{\gamma}^{\alpha}$ in the following form:

$$\dot{\gamma}^{\alpha} = \dot{\gamma}_{0}^{\alpha}\,\mathrm{sgn}(\tau^{\alpha})\left|\frac{\tau^{\alpha}}{g_{T}^{\alpha}}\right|^{n},$$
$$\tau^{\alpha} = \sigma_{ij}\mu_{ij}^{\alpha}, \tag{3}$$

where $\dot{\gamma}_{0}^{\alpha}$ is the reference strain rate, n is the rate sensitivity of the material, $\mathrm{sgn}(\blacksquare)$ is the signum function of $\blacksquare$ and g_{T}^{α} is the strength of the slip system α at the current time. In gradient plasticity, g_{T}^{α} is linked to strain gradients and expressed as

$$g_{T}^{\alpha} = g_{T}^{\alpha}\big|_{t=0} + \sqrt{(\Delta g_{S}^{\alpha})^{2} + (\Delta g_{P}^{\alpha})^{2}}, \tag{a) \quad (4}$$

$$\Delta g_S^\alpha = \sum_{\beta=1}^{N} h_{\alpha\beta} \Delta\gamma^\beta, \ \ \Delta g_P^\alpha = \alpha_T \mu_S \sqrt{b n_P^\alpha}, \tag{b}$$

$$h_{\alpha\alpha} = h_0 \operatorname{sech}^2 \left| \frac{h_0 \gamma}{g_T^\alpha \big|_{\text{sat}} - g_T^\alpha \big|_{t=0}} \right|, \ \ h_{\alpha\beta} = q h_{\alpha\alpha} (\alpha \neq \beta), \tag{c}$$

$$\gamma = \sum_\alpha \int_0^t \left| \dot{\gamma}^\alpha \right| dt,$$

$$n_P^\alpha = \left| \boldsymbol{m}^\alpha \times \sum_\beta s^{\alpha\beta} \nabla\gamma^\beta \times \boldsymbol{m}^\beta \right|. \tag{d}$$

In the MBSGCP theory, g_T^α equals to the sum of values of critical resolved shear stress ($CRSS = g_T^\alpha \big|_{t=0}$) determining initial shearing of the slip systems and the evolution of slip resistance during loading as a resultant of incremental hardening due to both SDs (Δg_S^α) and PDs (Δg_P^α) on the slip system α as described in Eq. (4a). In Eq. (4b) $h_{\alpha\beta}$, α_T, μ_S, b and n_P^α correspond to the hardening matrix, the Taylor coefficient, the shear modulus, the Burgers vector and the effective density of PDs at the current time, respectively. Here n_P^α has the dimension of [1/Length] deviating slightly from a more common definition of dislocation density - the total length of dislocation line per unit volume - with a dimension of [1/Length^2]. This difference arises from the fact that in this theory the definition of dislocation density is directly related to the strain gradient [40]. In the evaluation of the hardening moduli $h_{\alpha\beta}$ in Eq. (4c) [42], h_0 is the initial hardening parameter, $g_T^\alpha \big|_{\text{sat}}$ is the saturation stress of the slip system α at the current time, q is the latent hardening ratio and γ is the cumulative shear strain for all slip systems; on the other hand, in the evaluation of n_P^α in Eq. (4d), $\boldsymbol{m}^\alpha$ is the slip plane normal, $\boldsymbol{s}^\alpha$ is the slip direction with $s^{\alpha\beta} = \boldsymbol{s}^\alpha . \boldsymbol{s}^\beta$ and $\nabla\gamma^\beta$ is the gradient of shear strain in each slip system.

The performed micro-pillar compression experiments demonstrate that the yield strength of a pillar is inversely proportional to its edge length (or *S/V* ratio). In the MBSGCP theory, *CRSS* is solely dependent on the SDs, i.e. $g_T^\alpha \mid_{t=0} = g_S^\alpha \mid_{t=0}$, and it is a well known fact that the density of SDs is independent of the component's size; thus, it is unlikely to explain the size effect using this theory. In this paper an enhanced model of the MBSGCP theory is proposed, where the contribution of PDs is considered alongside that of SDs while determining the *CRSS* value of slip system based on experimental results. For instance, Maass et al. [24] investigated the initial microstructure of undeformed Au, Ni, Cu and NiTi micropillars using a white-beam Laue micro-diffraction technique and observed that GNDs/PDs existed in the initial microstructure of pillars.

An important question arised regarding the way to address the interaction of SDs and PDs in determination of the *CRSS* value. Columbus and Grujicic [43] proposed a functional form to describe the overall shear flow stress (τ_f) as a coupling between SDs and GNDs, $\tau_f = [(\tau_S)^\beta + (\tau_G)^\beta]^{1/\beta}$, where τ_S and τ_G correspond to shear flow stresses linked to SDs and GNDs, respectively, and β denotes the coefficient of coupling. In this study, we use a similar functional form to characterize the interaction between SDs and PDs in the calculation of *CRSS* as,

$$g_T^\alpha \mid_{t=0} = [(g_S^\alpha \mid_{t=0})^\beta + (g_P^\alpha \mid_{t=0})^\beta]^{1/\beta}, \qquad (5)$$

where $g_{\mathrm{S}}^{\alpha}|_{t=0}$ and $g_{\mathrm{P}}^{\alpha}|_{t=0}$ denote the contributions of SDs and PDs to the *CRSS*, respectively. These two terms are described in terms of the density of dislocations using an equation, similar to the Taylor's hardening law [44], as in the following:

$$g_{\mathrm{S}}^{\alpha}|_{t=0} = K\sqrt{\rho_{\mathrm{S}}|_{t=0}},$$

$$g_{\mathrm{P}}^{\alpha}|_{t=0} = K\sqrt{\rho_{\mathrm{P}}|_{t=0}} = K\sqrt{\rho|_{t=0}\left(\frac{\bar{S}}{\bar{V}}\right)^2},$$

(6)

where K is a constant, $\rho_{\mathrm{S}}|_{t=0}$ and $\rho_{\mathrm{P}}|_{t=0}$ are the densities of SDs and PDs, respectively and $\rho|_{t=0}$ is a reference density value used in the definition of PDs density. In Eq. (6) $\rho_{\mathrm{P}}|_{t=0}$ is correlated with the ratio of pillar's normalized surface ($\bar{S}$) to normalized volume ($\bar{V}$), where $\bar{S}$ and $\bar{V}$ correspond to the ratio of pillar's surface and volume to that of the largest pillar (pillar C), respectively. The normalization qualified this ratio to be dimensionless. Such a formulation complies with an experimental observation of Maass et al. [24], where a higher surface-to-volume ratio in micropillars was found to increase the occurrence of pre-existing GNDs (hence, PDs). This can be explained in the following way. During the manufacture of pillars (for instance, with a FIB technique) they become work-hardened; hence, finite stresses evolve in their body. Traction-free sides of pillars imply that certain stress components vanish on their surface. This inevitably leads to generation of sub-surface stress gradients, and, consequently, strain gradients, in the body. Considering different dimensions of pillars, in a smaller pillar, traction-free surfaces are situated closer to its axis; thus, strain gradients become more pronounced (numerically) in comparison to those in larger pillars. Thus, smaller pillars would generate higher PD densities demonstrating a

stronger response to deformation. Here we note that choosing a different pillar as the reference pillar would entail assuming a different value of $\rho|_{t=0}$ to ensure a constant $\rho_P|_{t=0}$. This does not affect the predictive capability of the proposed model.

Different β values were discussed in the literature [45]. For instance, $\beta=1$ corresponds to superposition of strengths due to SDs and PDs, i.e. $g_T^\alpha|_{t=0} = g_S^\alpha|_{t=0} + g_P^\alpha|_{t=0}$. Such a coupling was studied by Columbus and Grujicic [43]. On the other hand, $\beta=2$ corresponds to superposition of the density terms: $\rho_T|_{t=0} = \rho_S|_{t=0} + \rho_P|_{t=0}$. This approach was studied by several authors [3,46,47]. Here, $\beta=2$ was considered, thus strength of the slip system α at the current time is expressed as

$$g_T^\alpha = g_T^\alpha|_{t=0} + \Delta g_T^\alpha,$$

$$g_T^\alpha|_{t=0} = CRSS = \sqrt{(g_S^\alpha|_{t=0})^2 + (g_P^\alpha|_{t=0})^2} = K\sqrt{\rho_S|_{t=0} + \rho_P|_{t=0}}, \qquad \textbf{(7)}$$

$$\Delta g_T^\alpha = \sqrt{(\Delta g_S^\alpha)^2 + (\Delta g_P^\alpha)^2}.$$

Note that the EMSGCP theory is reduced to MBSGCP when $g_P^\alpha|_{t=0}$ vanishes and to the conventional crystal-plasticity (CP) theory when both $g_P^\alpha|_{t=0}$ and Δg_P^α are zero. The constitutive formulation of EMSGCP explained above was implemented in the implicit finite-element code ABAQUS/Standard using a user-defined subroutine. An important step in implementation was the determination of shear strain gradient $\nabla\gamma^\alpha$ in Eq. (4d). To compute this, first the shear strain values ($\gamma_n^{(\alpha)(i)}$) for each slip system, α, at each node within an element were obtained using the Abaqus user subroutine URDFIL, which reads the results file. Next, this data was transferred to the UMAT subroutine,

where the shear strain gradients at each integration point ($\nabla\gamma_{\mathrm{g}}^{(\alpha)(i)}$) are computed using the following equation [48]

$$\nabla\gamma_g^{(\alpha)(\mathrm{i})} = \frac{\partial\gamma_g^{(\alpha)(\mathrm{i})}}{\partial\mathbf{x}} = \frac{\partial\gamma_g^{(\alpha)(\mathrm{i})}}{\partial(\mathbf{\Psi})}\frac{\partial(\mathbf{\Psi})}{\partial\mathbf{x}} = \sum_{\mathrm{i}=1}^{8}\left(N^{\mathrm{i}}(\mathbf{\Psi})\nabla_{\mathbf{\Psi}}\right)\gamma_n^{(\alpha)(\mathrm{i})}\mathbf{J}^{-1},$$

where   **(8)**

$$\mathbf{J} = \frac{\partial\mathbf{x}}{\partial(\mathbf{\Psi})} = \sum_{\mathrm{i}=1}^{8}Y^i\left(N^{\mathrm{i}}(\mathbf{\Psi})\nabla_{\mathbf{\Psi}}\right),$$

is the Jacobian matrix, Y^i is the position of the integration points, $\mathbf{\Psi}$ is the vector of isoparametric coordinates of the Gauss integration point, $\nabla_{\mathbf{\Psi}}$ is the nabla operator relative to the isoparametric coordinate system, N^{i} is the shape function and $N^{\mathrm{i}}(\mathbf{\Psi})\nabla_{\mathbf{\Psi}}$ corresponds to the spatial derivative of shape functions. The relevant details can be found in [48-51].

4. Finite-element modelling of micro-pillar-compression experiments

A three-dimensional FE model of micropillar-compression experiment was developed to investigate the size effect in a single-crystal Ti-based alloy. Based on the experiments performed, a model accounting for the exact pillar's dimensions including the pillar's taper of 2.5° was developed. A schematic of the pillar geometry, finite-element discretization (of type C3D8 [52]) and the imposed boundary conditions are shown in Fig. 3. The dimensions of micro-pillars are given in Table 1. The aspect ratio (i.e. a ratio of height to the edge length) was kept between 2 and 2.4. The indenter was assumed to be a rigid body since the elastic modulus and yield strength of the diamond indenter is at least an order of magnitude higher than those for the Ti alloy under investigation. A relative movement of the indenter was imposed in the negative y-direction (Fig. 3). Kinematic boundary conditions were imposed on the bottom face of the pillars by

constraining displacements in all directions since the micro-pillars was tightly bonded to the underlying substrate. The validity of such a simplification was checked by comparing numerical results obtained from a pillar with a finite-size substrate (made of the same material). The results indicate minor variation in the stress distribution, confirming the overall accuracy of assuming a rigid substrate to reduce computational cost [53]. As the experimental study suggested, the $(121)[1\bar{1}1]$ was the dominant slip system in deformation [54]; only the set $\{112\}$ <111>, where $N = 12$, was enabled amongst the potential three systems in B.C.C. materials.

Fig. 3

Table 1

Elastic properties of the single-crystal Ti alloy were presented in Voigt notation, c_{11}, c_{12}, c_{44}. Determination of elastic parameters is a non-trivial process. Two sets of parameter values were obtained for two different temperature regimes (Table 2). The first set of elastic parameters was obtained from *ab-initio* simulations performed at 0 K for b.c.c. Ti alloys [55]. The second set was obtained from experimental results for the b.c.c. single-crystal titanium performed at high temperature (1273 K) using resonant-ultrasound spectroscopy experiment [56]. The shear modulus μ_S was calculated using the relation, $\mu_S = \sqrt{(c_{11} - c_{12}).c_{44}/2}$, proposed by Paufler [57]. The Burgers vector b in Eq. (4b) for b.c.c. metals equals to $a/2$ <111>, where a (=3.235 × 10^{-7} mm [55]) is the lattice parameter. Thus, $b = 2.802 × 10^{-7}$ mm. A dependence of elastic constants on temperature was studied for different metals by Varshni [58]. This study demonstrated that elastic constants decreased linearly with an increase in temperature except at very low temperatures (0-50 K) where an exponential change occured. As a first estimate, elastic parameter values at room temperature (300 K) were obtained via linear

interpolation. Calibrating the FE model for pillar experimental studies presented several challenges. Primarily, the presence of misalignments between the indenter and the pillar can severely affect the perceived value of elastic material properties [59]. Thus, the validity of linear interpolation in obtaining elastic parameter at room temperature was tested through numerical studies of nano-indentation experiments reported elsewhere [60]. Studies of nano-indentation demonstrated an excellent match between experiments and simulations for loading and unloading curves (F-d curves) [60,61].

Table 2

A mesh-sensitivity analysis was performed for pillar A using the EMSGCP theory. Average element size of 210 nm × 210 nm × 210 nm was sufficient in obtaining convergence in the macroscopic load-displacement response. However, the distribution of PDs was found to be mesh-size dependent. Similar observation was also reported by Cheong et al. [49] and Roy and Acharya [62]. The mesh element sizes were kept constant for all numerical experiments carried out in this study.

Coulomb's friction law was used to model the frictional interaction between the indenter tip and the pillar in the experiments. It is well known that the contact characteristics can significantly affect the deformation behaviour of components. In our study we consider three idealized friction conditions, with $\mu = 0$ representing a well lubricated indenter-workpiece interface followed by two dry (non-lubricated interface) contact conditions ($\mu = 0.05$ and 0.1). The value $\mu = 0.05$ was selected since a range of $0.03 \leq \mu \leq 0.06$ are often used to represent contact conditions at diamond-metal interface in the literature [59,63]. Additionally, $\mu = 0.1$ was considered to represent a dry contact condition. The pillar's lateral displacements at 10% nominal strain were compared for different contact conditions. It was observed in numerical simulations that

pillars with $\mu = 0$ and $\mu = 0.05$ buckled in compression, whereas the pillar with $\mu = 0.1$ deformed with no visible slippage as observed in Raabe et al. [64]. *In-situ* videos recorded during the compression experiments indicate that lateral slip of the pillar occured during the deformation process (Fig. 1). Thus, we choose $\mu = 0.05$ for the contact condition in simulations as $\mu = 0$ is physically unrealistic [59].

5. Calibration of parameters of EMSGCP model

In the proposed EMSGCP model, the incipient strain gradients contribute to the overall *CRSS* in the component, i.e. $g_{\mathrm{T}}^{\alpha}\big|_{t=0}$ is a function of $\rho_{\mathrm{S}}\big|_{t=0}$ and $\rho_{\mathrm{P}}\big|_{t=0}$. It is, however, difficult to characterize their individual contributions through the micro-pillar compression experiment. The proposed theory indicates that the influence of $g_{\mathrm{P}}^{\alpha}\big|_{t=0}$ on the *CRSS* vanishes with $\overline{S}/\overline{V} \to 0$ (Eq. (6)). In a nano-indentation experiment, where the indented workpiece material is of sufficiently large volumes in comparison to the exposed surface area, the effect of $g_{\mathrm{P}}^{\alpha}\big|_{t=0}$ on the *CRSS* may be assumed to be negligible. Hence, $\rho_{\mathrm{S}}\big|_{t=0}$ can be determined from the experiment. Thus, nano-indentation experiments were performed for different crystallographic orientations of the material resulting in $g_{\mathrm{S}}\big|_{t=0} = 150$ MPa and $\rho_{\mathrm{S}}\big|_{t=0} = 1.464 \times 10^{7}$ mm^{-2}. Details of the models developed are available elsewhere [60,66]. It should be noted that the inelastic parameters α_{T} and h_{0} were also identified using nano-indentation experiments (Table 3). Next, micro-pillar compression experiments were used to callibrate $\rho_{\mathrm{P}}\big|_{t=0}$ for different pillar sizes. Through multiple trials, an agreement between the experimental and calculated average stress-strain curves was, with $\rho\big|_{t=0} = 1.510 \times 10^{7}$ mm^{-2}. Using Eq. (6), $g_{\mathrm{P}}^{\alpha}\big|_{t=0}$ can be calculated for different geometries. The $\overline{\sigma}$ - $\overline{\varepsilon}$ plot for pillars A, B and C show a significant deviation from the experiments (Fig. 4a). This was believed to be due

to a misalignment between the indenter tip and the pillar's top surface as it is difficult to ensure a perfect alignment in the experiment [59]. By introducing a misalignment of 6° (tilt about the z-axis) in the numerical experiments, an excellent match is obtained for the pillars studied (Fig. 4b-d).

Table 3

Fig. 4

Fig. 5

Next, a case study was performed, where a cylindrical pillar with diameter of 0.955 μm and height of 2.73 μm, made of the same material and oriented in the same direction was compressed to examine, (1) accuracy of the proposed EMSGCP theory and, (2) universality of the theory for different pillar geometries. As demonstrated in Fig. 5, a noticeable deviation from experiments is observed for the FE simulation assuming ideal geometrical configuration of the pillar. However, by introducing a misalignment of 2.5° an excellent match was obtained between the experiment and the simulation until about 2.2% strain. Beyond this, the flow curves start to diverge, i.e. geometrical softening observed in the experiment was not captured in the simulation. It is to be noted that geometrical softening observed in the experiments and simulations are not similar to each other. In the experiment, the upper surface of the pillar starts to slip w.r.t. the indenter's tip, and at some instance, a part of the pillar begins to shear off at a certain plane (Fig. 1d). This leads to a loss of reaction force imposed on the indenter as well as change in the geometric cross-sectional area. Consequently, in the simulations, there is no mechanism to capture material tearing, which leads to the deviation. In summary, we observe that presence of misalignment, however small, in pillar compression tests has a significant effect on the perceived deformation response. Here,

the misalingnment is modelled as a calibration constant using the technique demonstrated.

6. Numerical predictions of size effect in pillars and discussions

In this section, size effect in single-crystal Ti alloy is studied in idealised geometric configurations, i.e. neglecting pillar taper and misalignment. Pillars with a square cross-section with an edge length of 1, 2, 4, 8, 16 and 32 μm were modelled. The height-to-edge length aspect ratio was fixed at 2.1:1 in all the models. Consistent with the mesh-sensitivity analysis performed in Section 4, the mesh size of 210 nm × 210 nm × 210 nm was used to discretize the pillars. The crystal orients with the micro-pillar axis coinciding with the (010) direction.

Table 4

The numerically obtained stress-strain curves for Ti micropillars D, E, F, G and H are compared in Fig. 6a. Consistent with the *CRSS* values in Table 4, the yield strength of the micropillars is observed to increase with a decreasing pillar size, providing evidence of a strong size effect. It may be noted that the phenomenon is more pronounced for pillars of smaller sizes compared to those of larger ones. This Fig. also suggests that there is minimal 'size effect' for pillars G and H since their flow curves are almost identical, implying that the effect of initial microstructure for both pillars is similar. The flow curve of pillar H is a lower bound for all the flow curves since the *CRSS* value of 151.44 MPa is close to the corresponding value of 150 MPa, obtained from the nano-indentation experiments [60], where the influence of incipient strain gradients was negligibly small. Our results demonstrate that below an edge length of 8 μm the "smaller is stronger" phenomena is observed. This edge length is therefore considered

as the critical edge length, l_c, above which the relative change in the corresponding stress value is less than 5%.

In cylindrical pillars, the value of critical resolved shear stress can be scaled with respect to the diameter d of the micro-pillar using the following power-law form

$$\frac{CRSS}{\mu_s} = A \left(\frac{d}{b} \right)^M ,$$

(9)

where μ_s is the shear modulus and A and M are constants. Dou and Derby [39] obtained these constants, A=0.71 and M=-0.66, by using a least-squares fit to the experimental data for f.c.c. metal pillars. Here we consider d=d_{eff}. The corresponding curve for Ti alloy is shown in Fig. 6b. From the logarithmic plot, the constants were determined to be A =0.72 and M =-0.41.

The proposed theory accounts for PDs evolving during the deformation process. To demonstrate the contribution of evolution of PDs to local hardening of the material in EMSGCP, an enhanced model of crystal-plasticity (EMCP) was introduced that accounts for the density of PDs in the experimental samples but not PDs evolving in the course of deformation. This model is derived from the proposed EMSGCP theory by setting $\Delta g_P^\alpha = 0$ in Eq (7). A comparison with the EMSGCP theory elucidates the level of strain gradients evolving during the deformation process (Fig. 6a, pillars D and E). As expected, in the EMSGCP theory the strain-hardening rate is higher due to evolution of strain gradients during deformation. To quantify this effect as a function of pillar size, the work-hardening rate (WHR), defined as a slope of the curve between strains of 15% and 20%, for pillars D, E, F and G was determined. The respective values are 981 MPa (Pillar D), 659 MPa (Pillar E), 480 MPa (Pillar F) and 229 MPa (Pillar G). Interestingly,

a significant increase in WHR is observed with a decreasing pillar size, with WHR $\propto$ $(d_{\text{eff}})^{-0.675}$. These results demonstrate that with a decreasing pillar size, higher strain gradients evolve during deformation.

Fig. 6

The distributions of evolving strain gradients for different pillar sizes were also investigated. Instantaneous plastic strain in the loading directions (ε_{22}) at the mid-plane of pillars D, E and F at the end of the loading step (nominal strain of ~ 27%) was compared; Fig. 7a demonstrates the similarity of the strain distribution in a normalised scale. The distributions of the sum of the magnitudes for the effective PD density for all the slip systems ($\sum \left| n_P^{(\alpha)} \right|$) are shown in Fig. 7b. They indicate that PDs were significant in pillar D, modest in pillar E and lowest in pillar F. It was found that PDs tended to accumulate between the middle and the lower end of the pillars' mid-plane since variations in total shear-strain values were more pronounced in these regions. Since the primary deformation occurred in the loading direction (with respect to the flat indenter), the total shear strain from all the slip systems was essentially indentical to the distribution of accumulated plastic strain in the loading direction, ε_{22}. Therefore, the variation in ε_{22} (i.e. strain gradients) can be correlated with effective density of PDs in all slip systems ($\sum \left| n_P^{(\alpha)} \right|$). It should be emphasized that although the strain distributions in pillars of different sizes were similar, their gradients, i.e. their variation through the dimensions, are different. These results demonstrate that in smaller pillars higher strain gradients evolve during deformation.

Fig. 7

In micro-pillar-compression experiments, although the deformation is applied uniaxially, heterogeneity evolves in the course of loading due to imposed boundary conditions. To demonstrate this, the bottom surface of Pillar D was constrained in the loading direction (i.e. $u_2 = 0$). Rigid body modes were eliminated by constraining the centre node of the

pillar's bottom surface in all directions. This resulted in homogenous, uniform distributions of uniaxial strain and stress in the body, which, in turn, generates no gradients of plastic strain (Fig. 8a). The respective distribution for the model with the bottom surface fixed in all directions (shown in Fig. 8b) demonstrate that the heterogeneous deformation develops in the component as a result of the imposed boundary conditions leads to evolution of strain gradients.

Fig. 8

7. Case study: Sensitivity of l_c

In this section sensitivity of the length-scale parameter, l_c, to material parameters, i.e. *CRSS*, *K* and *β*, is studied. Since *CRSS* (or $g_T^\alpha \mid_{t=0}$) is a function of the incipient densities of SDs ($\rho_S \mid_{t=0}$) and PDs ($\rho_P \mid_{t=0}$) (see Eq. (7)), different cases were considered for varying relative magnitudes of ρ_S and ρ_P. In addition to already determined values of densities presented in Table 3, two cases with different density levels were also analysed for independent variations of these two parameters. In the first case $\rho_S \mid_{t=0}$=7.0×10^6 mm^{-2} while $\mid_{t=0}$=1.510×10^7 mm^{-2} (as before) and in the second case $\mid_{t=0}$=5.0×10^6 mm^{-2} while $\rho_S \mid_{t=0}$=1.464×10^7 mm^{-2} (as before). The change in the *CRSS* value with the edge length of pillars is shown in Fig. 9a. Here 'Present' refers to the dislocation densities as per Table 3. The results indicate that the critical edge length depends on the initial dislocation density of the material. This suggests that a decrease in $\rho_S \mid_{t=0}$ and/or an increase in $\rho_P \mid_{t=0}$ lead to an increase in l_c; as a result, the size effect is observed for a larger range of pillar sizes.

Fig. 9

The sensitivity of l_c to other material properties, namely, K and β, was also studied. The initial strength of slip system to the incipient density of dislocations was correlated via K, while β represents the sensitivity of coupling between $\rho_S|_{t=0}$ and $\rho_P|_{t=0}$. In addition to $K = 0.04$ MPa mm, $K = 0.02$ MPa mm and 0.08 MPa mm were considered. The *CRSS* values for pillars D to I as a function of their edge length in a logarithmic scale are shown in Fig. 9b. This plot indicates that l_c is 8 μm for all K values, implying that l_c is not sensitive to parameter K for the range studied.

Next $\beta = 1$ and 2 were considered with $K = 0.04$ MPa.mm. Fig. 9c demonstrates the corresponding *CRSS* value for pillars D to I as a function of their edge length. The plot suggests that $l_c = 64$ μm for $\beta = 1$. It should be noted that the *CRSS* value of the pillar with dimensions of 64 μm × 64 μm × 134.4 μm was also checked. It demonstrated a difference of less than 5% in the *CRSS* value compared to corresponding value of pillar I, thus justifying that $l_c = 64$ μm for $\beta = 1$. This analysis suggests that an increase in the β value leads to a decrease in l_c. Some prior studies (Abu Al-Rub and Voyiadjis, 2004) demonstrated that a smaller interaction coefficient β implied increased interaction between SDs and GNDs. Based on this, it can be concluded that the stronger interaction of incipient SDs and incipient PDs leads to a larger range of pillar sizes demonstrating the size effect.

8. Concluding remarks

In this paper, we propose an enhanced model of strain-gradient crystal plasticity, with the incipient strain gradients correlated with the sample's surface-to-volume ratio, based on experimental evidence. Predictive capabilities of the model in characterizing the size effect in the initial yield and the work-hardening rate (including distributions of

evolving strain gradients) in small-scale components with different geometries are demonstrated. The proposed model has two additional parameters compared to standard strain-gradient crystal plasticity theories. One of these parameters (K) represents the effect of the Taylor factor and the other (β) couples the instantaneous densities of polar dislocations and statistical dislocations to the material's strength. In the micro-pillar compression studies, heterogeneity evolves in the pillar due to the imposed boundary conditions. The strain variation in smaller pillars is higher compared to that in larger pillars, resulting in a harder response.

By way of calibrating the model, indentation and micropillar compression tests were carried out. Based on the calibrated model, uniaxial compression tests in pillars of square and circular cross-sections were simulated. The influence of minor misalignments on the overall stress-strain response was noted. It was also demonstrated that the critical edge length, below which size effect was observed, was sensitive to the densities of PDs and SDs and the coupling co-efficient (β).

The proposed model may be employed to study a variety of boundary-value problems in the small scale. For example, deformation in thin films can be attempted. In this case, the *S/V* ratio is inversely proportional to the film thickness. This implies that with decreasing film thickness we expect to see a harder response (which is experimentally observed).

Through this paper, we demonstrate a practical way of justifying the observation from experiments in the small length-scales. Though the proposed continuum model is phenomenological, we make a conscious effort to demonstrate the physical justification of our model by taking inspiration from experimental studies.

References

[1] Fleck NA, Muller GM, Ashby MF, Hutchinson JW. Acta Metallur Mater 1994;42:475-87.

[2] Stölken J, Evans A. Acta Mater 1998;46:5109-15.

[3] Ma Q, Clarke DR. J Mater Resear 1995;10:853-63.

[4] Uchic MD, Dimiduk DM, Florando JN, Nix WD. Science 2004;305:986-89.

[5] Greer JR, Oliver WC, Nix WD. Acta Mater 2005;53:1821-30.

[6] Gurtin ME, Anand L. Model Sim Mater Sci Eng 2006;15(1):S263.

[7] Dimiduk D, Uchic M, Parthasarathy T. Acta Mater 2005;53:4065-77.

[8] Ng KS, Ngan AH. Model Sim Mater Sci Eng 2008; 16(5):055004.

[9] Greer JR, Nix WD. Phys Rev B 2006;73:245410.

[10] Parthasarathy TA, Rao SI, Dimiduk DM, Uchic MD, Trinkle DR. Scr Mater 2007;56:313-16.

[11] Rao SI, Dimiduk DM, Parthasarathy TA, Uchic MD, Tang M, Woodward C. Acta Mater 2008;56:3245-59.

[12] Norfleet DM, Dimiduk DM, Polasik SJ, Uchic MD, Mills MJ. Acta Mater 2008;56:2988-3001.

[13] El-Awady JA, Wen M, Ghoniem NM. J Mech Phys Solids 2009;57:32-50.

[14] Bei H, Shim S, Miller M, Pharr G, George E. Appl Phys Lett 2007;91:111915.

[15] Kiener D, Motz C, Rester M, Jenko M, Dehm G. Mater Sci Eng A 2007;459:262-72.

[16] Jennings AT, Burek MJ, Greer JR. Phys Rev Lett 2010;104:135503.

[17] Maaß R, Van Petegem S, Grolimund D, Van Swygenhoven H, Kiener D, Dehm G. Appl Phys Lett 2008;92:071905.

[18] Maaß R, Van Petegem S, Borca C, Van Swygenhoven H. Mater Sci Eng A 2009;524:40-45.

[19] Maaß R, Van Petegem S, Van Swygenhoven H, Derlet PM, Volkert CA, Grolimund D. Phys Rev Lett 2007;99:145505.

[20] Guruprasad P, Benzerga A. J Mech Phys Solid 2008;56:132-56.

[21] Kuroda M, Tvergaard V. Int. J. Solid. Struct. 2009;46:4396-4408.

[22] Akarapu S, Zbib HM, Bahr DF. Int J Plast 2010;26:239-57.

[23] Zhang X, Aifantis K. Mater Sci Eng A 2011;528:5036-43.

[24] Maaß R, Van Petegem S, Zimmermann J, Borca C, Van Swygenhoven H. Scr Mater 2008;59:471-74.

[25] Fan H, Li Z, Huang M. Scr Mater 2012;67:225-28.

[26] Hurtado DE, Ortiz M, J Mech Phys Solid 2012;60:1432-46.

[27] Acharya A. J Mech Phys Solid 2001;49;761-85.

[28] Fressengeas C, Taupin V, Capolungo L. Int J Solid Struct 2011;48:3499-3509.

[29] Puri S, Roy A. Comp Mater Sci 2012;52:20-24.

[30] Puri S, Das A, Acharya A. J Mech Phys Solid 2011;59:2400-17.

[31] Nye JF. Acta Metall 1953;1.2:153-162.

[32] Kröner E. Erg Angew Math 1958;5:1-

[33] Taupin V, Varadhan S, Fressengeas C, Beaudoin AJ. Acta Mater 2008;56:3002-3010.

[34] Acharya A, Roy A. J Mech Phys Solid 2006;54:1687-.

[35] Rabe R, Breguet JM, Schwaller P, Stauss S, Haug FJ, Patscheider J, Michler J. Thin Solid Films 2004;469;206-13.

[36] Ghisleni R, Rzepiejewska-Malyska K, Philippe L, Schwaller P, Michler J. Microsc res tech 2009;72:242-49.

[37] Sun Q, Guo Q, Yao X, Xiao L, Greer JR, Sun J. Scr Mater 2011;65:473-76.

[38] Frick CP, Clark BG, Orso S, Schneider AS, Arzt E. Mater Sci Eng A 2008;489:319-29.

[39] Dou R, Derby B. Scr Mater 2009;61:524-27.

[40] Han C, Gao H, Huang Y, Nix WD. J Mech Phys Solid 2005;53:1188-1203.

[41] Hutchinson J. Proc Royal Soc London A Math Phys Sci 1976;348:101-27.

[42] Peirce D, Asaro R, Needleman A. Acta Metallur 1982;30:1087-1119.

[43] Columbus D, Grujicic M, Mater Sci Eng A 2002;323:386-402.

[44] Taylor SGI. Plastic strain in metals 1938.

[45] Abu Al-Rub RK, Voyiadjis GZ. Int J Plast 2004;20:1139-82.

[46] Ashby M. Phil Mag 1970;21:399-424.

[47] Stelmashenko N, Walls M, Brown L, Milman YV. Acta Metallurgica et Mater 1993;41:2855-65.

[48] Busso EP, Meissonnier FT, O'Dowd NP. J Mech Phys Solid 2000;48:2333-61.

[49] Cheong KS, Busso EP, Arsenlis A. Int J Plast 2005;21:1797-1814.

[50] Lee WB, Chen YP, Int J Plast 2010;26:1527-40.

[51] Siddiq A, Schmauder S, Huang Y. Int J Plas 2007;23:665-89.

[52] Systemes D. Abaqus 6. 11 Analysis User Manual 2011.

[53] Jérusalem A, Fernández A, Kunz A, Greer JR. Scr Mater 2012;66:93-96.

[54] Nowag K. PhD Thesis: Deformation mechanisms of hard to machine metal Alloys at the micro scale, 2013. EMPA, Switzerland.

[55] Tegner BE, Zhu L, Ackland GJ. Phys Rev B 2012;85:214106.

[56] Ledbetter H, Ogi H, Kai S, Kim S, Hirao M. J Appl Phys 2004;95:4642.

[57] Schulze D, Paufler P. GER Schulze, Physikalische Grundlagen mechanischer Festkörpereigenschaften. Bünde 229 (I) und 238 (II) der wiss. Taschenbücher, Akademie-Verlag, Berlin 1978 143 bzw. 190 Seiten, 50 bzw. 100 Abbildungen, 16 bzw. 19 Tabellen, Preis je Band 8,-M: Kristall und Technik 1978;14:K42.

[58] Varshni Y. Phys Rev B 1970;2:3952-58.

[59] Zhang H, Schuster BE, Wei Q, Ramesh KT. Scr Mater 2006;54:181-86.

[60] Demiral M, Roy A, Silberschmidt VV. Comp Mater Sci 2013;79:896-902.

[61] Demiral M. Enhanced gradient crystal-plasticity study of size effects in b.c.c. metal, 2012 PhD thesis, Loughborough University, UK.

[62] Roy A, Acharya A. J Mech Phys Solid 2006;54:1711-43.

[63] Spear KE, J American Ceramic Soc 1989;72:171-91.

[64] Raabe D, Ma D, Roters F. Acta Mater 2007;55: 4567-83.

[65] Demiral M, Roy A, El Sayed T, Silberschmidt VV. Mater Sci Eng A 2014;608:73-81.

[66] Huang Y. A user-material subroutine incorporating single crystal plasticity in the ABAQUS finite element program, Mech Report 178 1991.

[67] Kysar J. Addendum to 'A user-material subroutine incorporating single crystal plasticity in the ABAQUS finite element program: Mech Report 178', 1997, Division of Engineering and Applied Sciences, Harvard University, Cambridge, MA.

Tables

Table 1: Geometric details of micro-pillars in experiments

Pillar	Pillar dimensions (width × length × height, μm)	$S/V\,(\mu m^{-1})$
A	$1.080 \times 0.920 \times 2.120$	4.154
B	$1.640 \times 1.770 \times 3.760$	2.410
C	$2.030 \times 1.970 \times 4.680$	2.032

Table 2: Elastic constants for Ti alloy from different sources

	T (K)	c_{11} (GPa)	c_{12} (GPa)	c_{44} (GPa)	μ_s (GPa)
Ab-initio simulations	0	137.00	130.00	46.00	12.68
Experiments	1273	97.70	82.70	37.50	16.77
Interpolated (linearly)	300	127.74	118.85	43.99	13.98

Table 3: Parameters of enhanced strain-gradient crystal-plasticity model

CP parameters	SGCP parameters	EMSGCP parameters
$\dot{\gamma}_o^\alpha = 10^{-4}\ \text{s}^{-1}$	$\alpha_T = 0.7$	$\beta = 2$
$n = 15$	$b = 2.802 \times 10^{-7}\ \text{mm}$	$K = 0.0392\ \text{MPa.mm}$
$q = 1$		$\rho_S|_{t=0} = 1.464 \times 10^7\ \text{mm}^{-2}$
$h_0 = 10\ \text{GPa}$		$\rho|_{t=0} = 1.510 \times 10^7\ \text{mm}^{-2}$
		S/V (see Table 1)

Table 4: EMSGCP parameters for different sizes of pillars

Pillar type	Pillar dimensions (width × length × height, μm)	$\bar{S}/\bar{V}$	$\rho_G|_{t=0}$ (10^7mm^{-2})	$g_T^\alpha|_{t=0}$ (MPa)
D	$1 \times 1 \times 2.1$	2.202	7.321	367.54
E	$2 \times 2 \times 4.2$	1.101	1.830	225.04
F	$4 \times 4 \times 8.4$	0.551	0.457	171.85
G	$8 \times 8 \times 16.8$	0.275	0.115	155.74
H	$16 \times 16 \times 33.6$	0.138	0.028	151.44
I	$32 \times 32 \times 67.2$	0.069	0.007	150.35

Figures
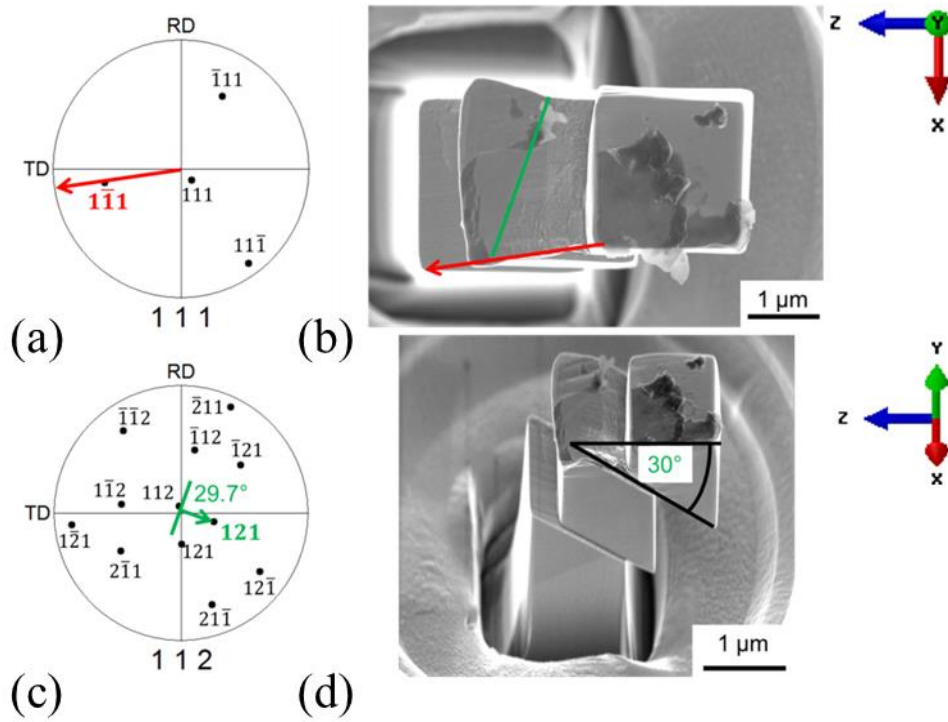
Fig. 1: Determination of active slip system by comparing EBSD pole Fig.s for {111} (a) and {112} directions (c) with SEM images for pillar C (see Table 1) taken after compression from top (b) and under 45° tilt (d, dimensions corrected for tilt). The active slip system was found to be (121)[1 $\bar{1}$ 1].
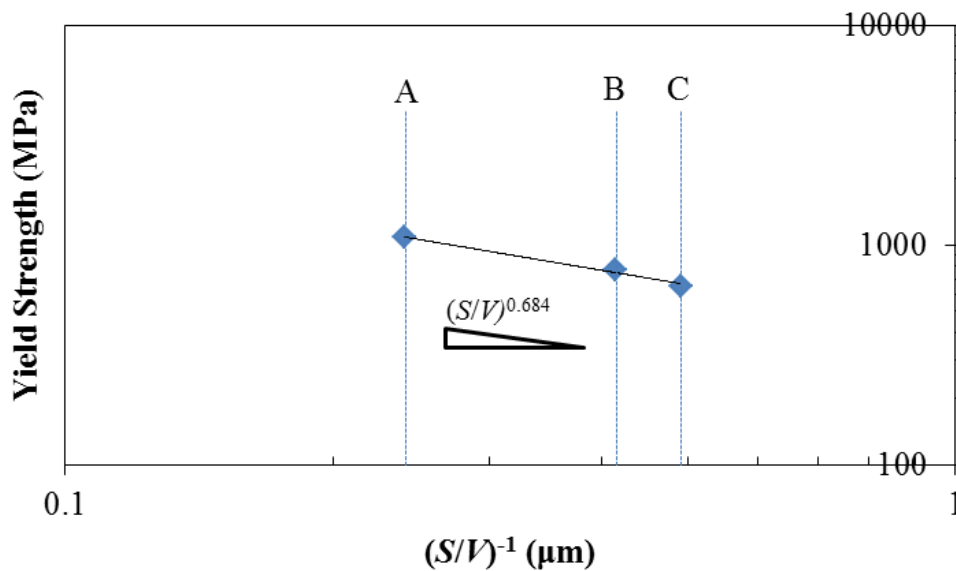
Fig. 2: Logarithmic plot of yield strength vs. inverse surface-to-volume ratio for pillars A, B and C. The solid line represents the best-fit power-law function.
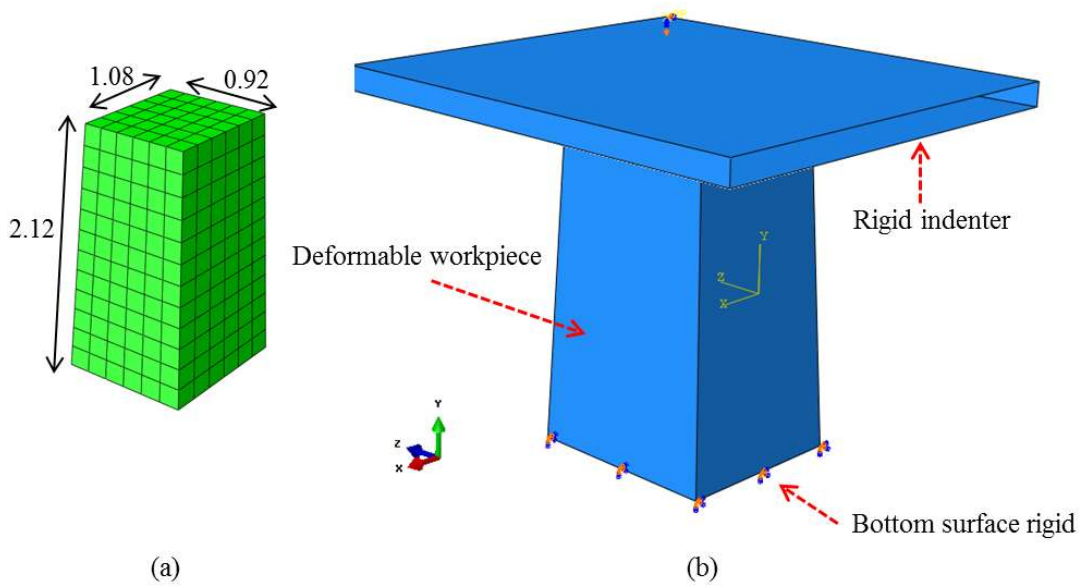
(a)   (b)

Fig. 3: (a) Dimensions of micropillars (in µm); (b) 3D model of micro-pillar-compression experiment
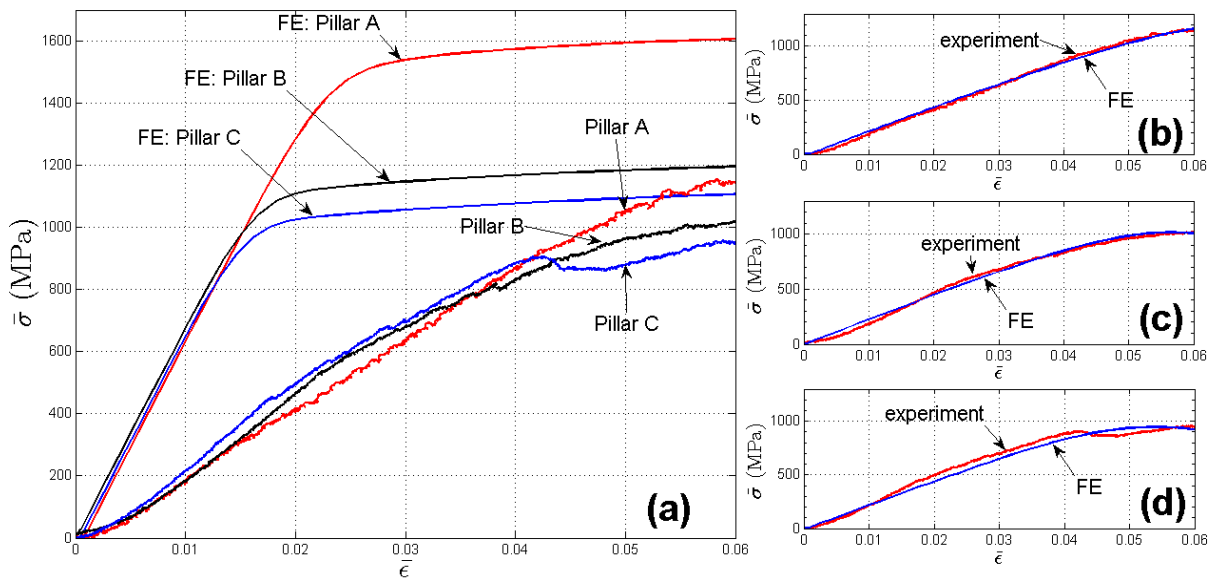
Fig. 4: Average stress-strain curves obtained from experiments and FE simulations of pillars A, B, C using EMSGCP theory
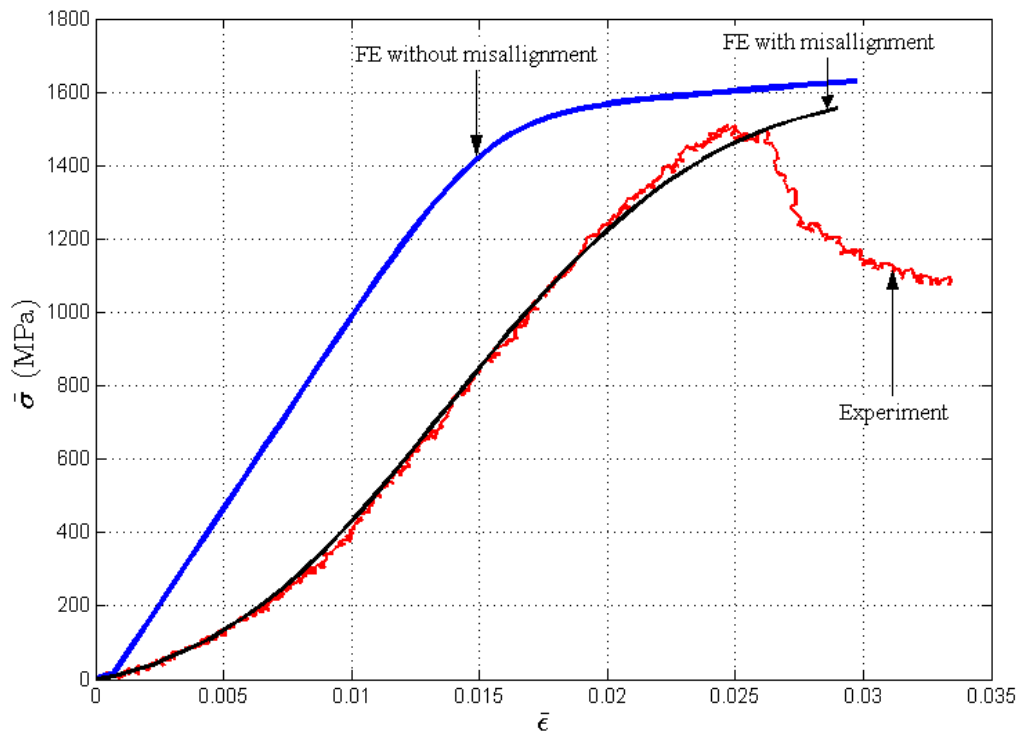
Fig. 5: Average stress-strain curves obtained from experiments and FE simulations of cylindrical pillar using EMSGCP theory
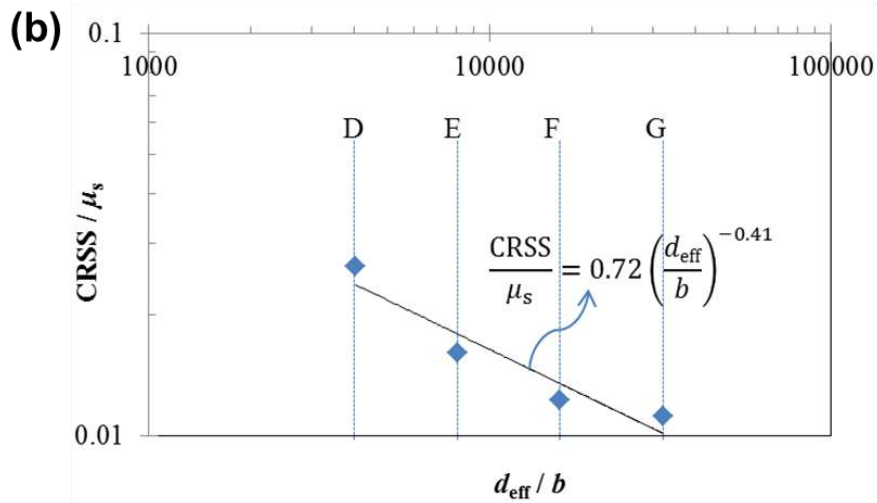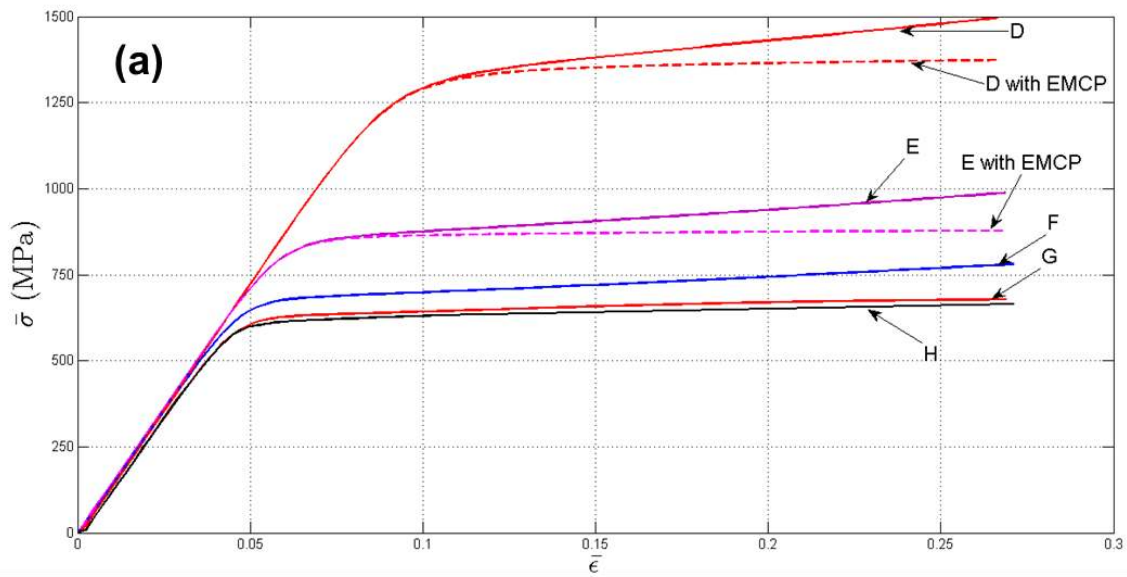
Fig. 6: (a) True stress-strain curves obtained with FE simulations using EMSGCP theory for pillars D, E, F, G and H and CP theory for pillars D and E. (b) Logarithmic plot of CRSS (normalized with μ_s) vs. d_{eff} (normalized with b) for pillars D, E, F and G
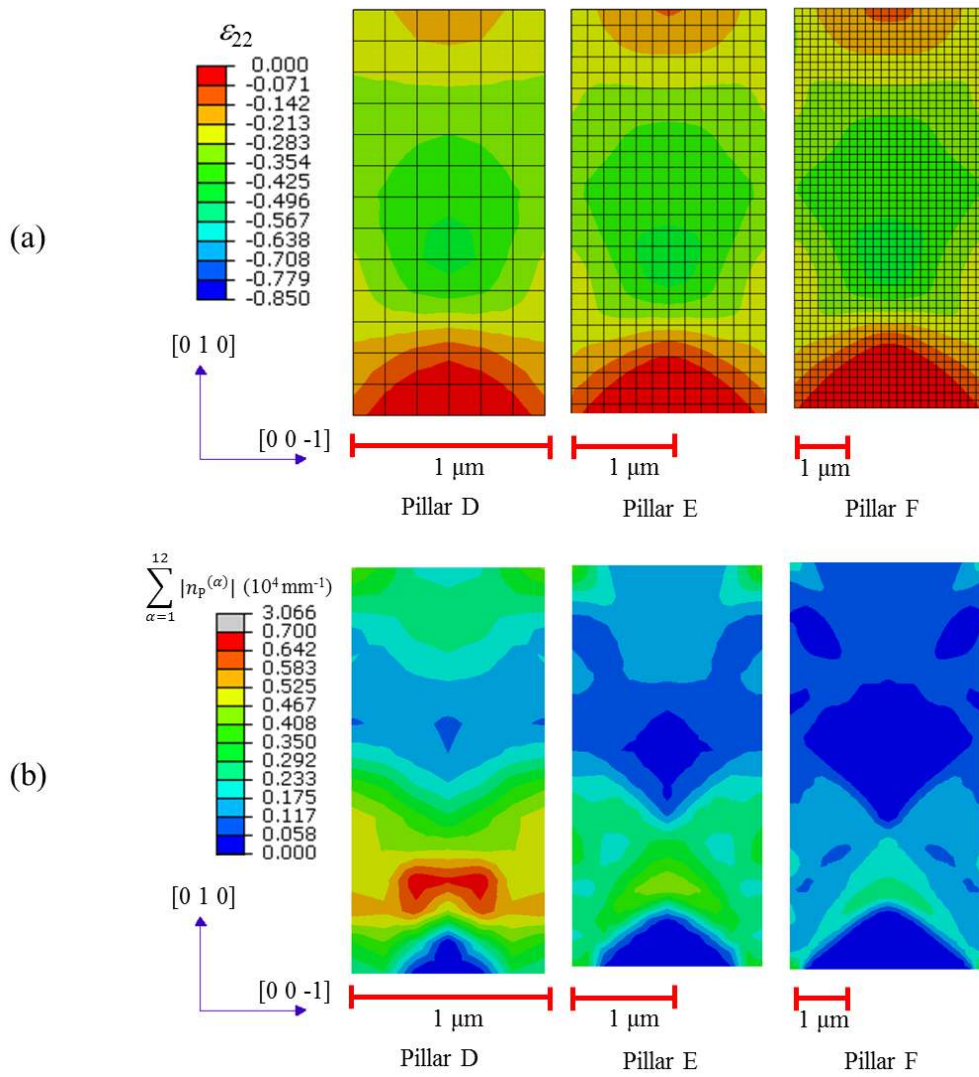
Fig. 7: Distribution of accumulated plastic strain in loading direction (a) and effective density of PDs in all slip systems (b) at full loading obtained with FE simulations for mid-plane of pillars D, E and F (consider different length scales)
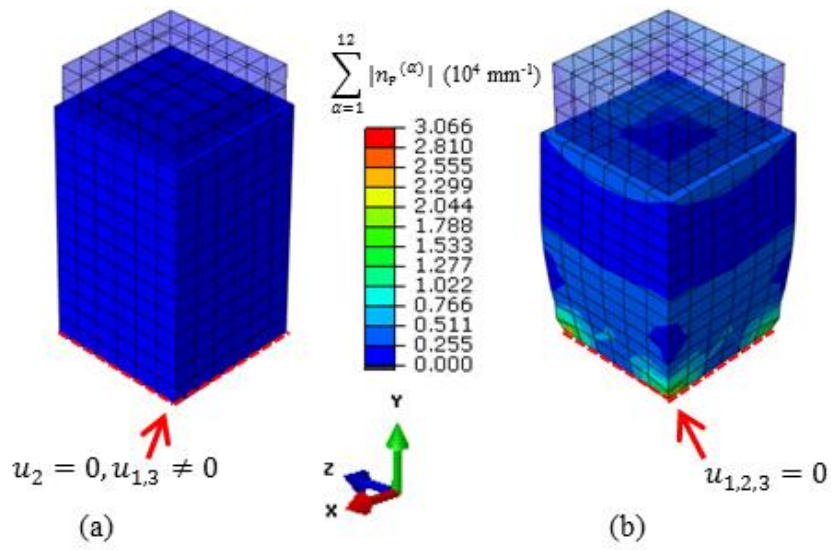
Fig. 8: Distribution of effective density of PDs in all slip systems ($\sum \left| n_{\mathrm{P}}^{(\alpha)} \right|$) for pillar D when the bottom surface is fixed only in loading direction (a) and in all directions (b)
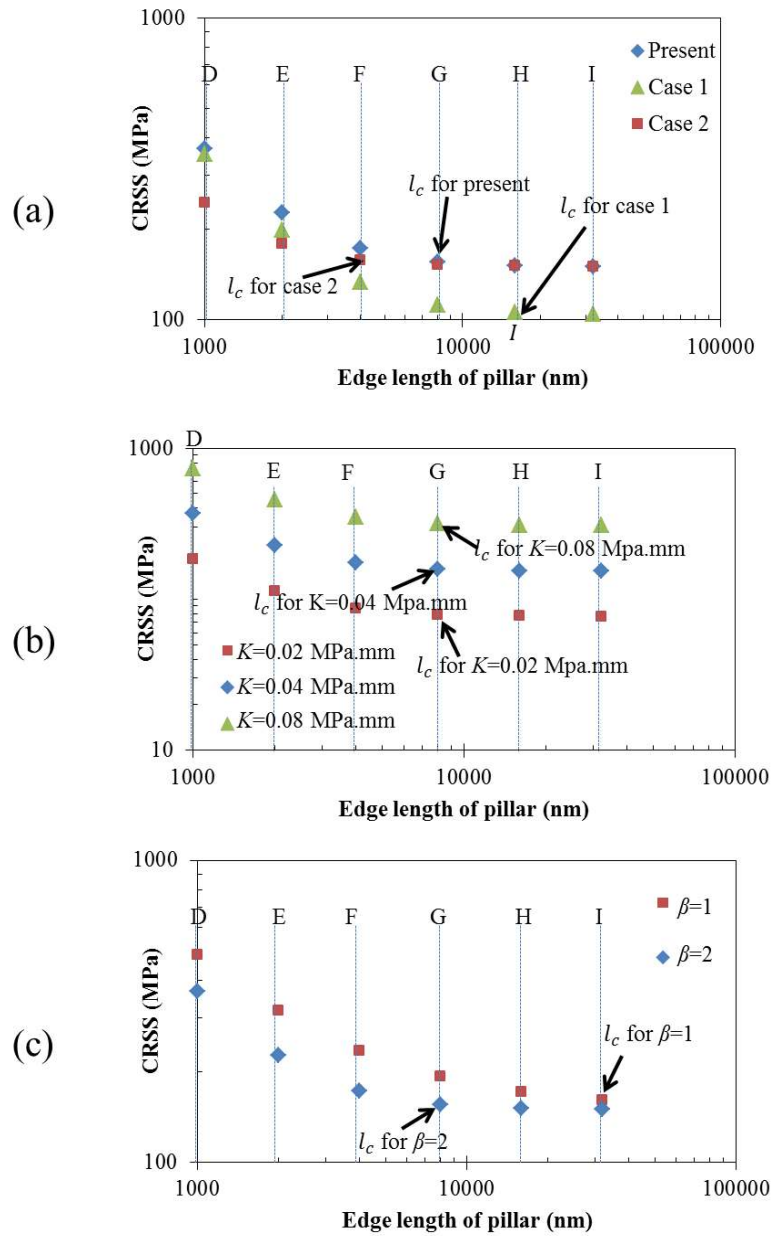
Fig. 9: Logarithmic plots of resolved shear stress vs. edge length of pillar for different cases (a), K values (b) and β values (c)